

A review on East Asian dust storm climate, modelling and monitoring

Y. Shao ^{a,*}, C.H. Dong ^b

^a Dept. of Physics and Materials Science, City University of Hong Kong, Hong Kong SAR, China

^b National Satellite Meteorology Centre, China Meteorological Administration, Beijing, China

Received 27 April 2005; accepted 9 February 2006

Abstract

In arid and semi-arid area of Asia, dust storms occur frequently. Asian dust storms have a major impact on the air quality of the densely populated areas of China, Korea and Japan, and are important to the global dust cycle. In extreme cases, they result in the loss of human lives and disruptions of social and economic activities. In recent years, systematic research on Asian dust storms has been carried out. Much progress has been made in the development of integrated dust storm monitoring and modeling systems by making use of advanced numerical models, satellite remote sensing and GIS data. In this paper, we summarize the recent achievements in Asian dust storm research with an emphasis on dust climatology, modeling and satellite monitoring. The concept of integrated dust storm monitoring and modeling system is described and a summary of the developments in key research areas is given, including new dust models and techniques in satellite remote sensing and system integration. We then discuss the current research frontiers and the challenges for future studies.

© 2006 Elsevier B.V. All rights reserved.

Keywords: Dust storms; Dust storm modeling; Dust storm monitoring; Satellite remote sensing; Asian dust

1. Introduction

In China, arid and semiarid areas occupy 3.57 million km², consisting of 0.253, 1.427, 1.139 and 0.751 million km² hyper-arid, arid, semiarid and dry sub-humid lands, respectively. Distributed from west to east are the Taklamakan, Gurbantunggut, Tsaidam Basin, Kumutage, Badain Juran, Tengger, Ulan Buh, Hobq, Mu Us Deserts and other smaller deserts. A large portion of Mongolia is occupied by desert plains and southeast Mongolia is part of the Gobi. Over these vast areas, dust storms are frequent and sometimes severe, especially in late spring to early summer. The dust storms are referred

to as East Asian Dust Storms, or simply Asian dust storms in the literature. Prospero et al. (2002) identified 9 potential dust source regions around the globe and it seems appropriate to call dust storms according to the source regions. In recent years, Asian dust storms have been a focus of several major research projects (e.g., Arimoto et al., 2006; Mikami et al., 2006).

Much progress has been made in the monitoring, modeling and prediction of Asian dust storms. Of particular importance is the development of integrated dust-storm monitoring and modeling systems on the basis of numerical models, satellite remote sensing, synoptic observations and GIS (Geographic Information System) data. In this paper, we summarize the recent achievements in Asian dust storm research, including the understanding of Asian dust storm climatology

* Corresponding author.

E-mail address: y.shao@cityu.edu.hk (Y. Shao).

(Section 2), integrated dust storm modeling systems (Section 3) and dust storm monitoring through satellite remote sensing (Section 4). In the final section of the paper, we discuss the issues which require further study.

2. Asian dust storm climatology

2.1. Dust storm distribution and frequency

Asian dust storm climatology is quite well documented through the analyses of synoptic records over the past 50 years (Sun et al., 2001; Zhou, 2001; Chun et al., 2001; Qian et al., 2002; Natsagdorj et al., 2003; Kurosaki and Mikami, 2003; Shao and Wang, 2003) and of satellite data of recent years (e.g., Prospero et al., 2002). According to the WMO (World Meteorological Organisation) protocol, dust events are classified according to visibility into the categories of:

- (1) Dust-in-Suspension: widespread dust in suspension, not raised at or near the station at the time of observation; visibility is usually not greater than 10 km;
- (2) Blowing Dust: raised dust or sand at the time of observation, reducing visibility to 1 to 10 km;
- (3) Dust Storm: strong winds lift large quantities of dust particles, reducing visibility to between 200 and 1000 m; and
- (4) Severe Dust Storm: very strong winds lift large quantities of dust particles, reducing visibility to less than 200 m.

In dust-affected areas in Asia, synoptic observations are made at a large number of weather stations at 3-hourly intervals over the past 50 years or so. This dataset (or subsets) of the synoptic data has been used to study dust storm frequency distribution and the synoptic systems for dust storm generation. It is worth pointing out that in practice the classification of dust events is somewhat subjective and observers from different countries have different preferences in preparing the synoptic reports.

Sun et al. (2001) analyzed the synoptic reports over the 40-year period between 1960 and 1999 and found the Gobi in Mongolia and north China (around 95–114°E, 37–45°N) is a major dust source. The region of highest dust-event frequency is the Hexi Corridor (105–110°E, 38–42°N). In a similar analysis, Zhou (2001) identified the Tarim Basin together with the adjacent areas and the Alashan, Ordos and Hexi Corridor regions as the two main dust centers in China. Natsagdorj et al. (2003) studied dust activities in Mongolia by analyzing

the distributions of strong dust events (dust storm plus severe dust storm) and weak dust events (dust-in-suspension plus blowing dust) using a composite of synoptic data between 1937 and 1999. They found the dust-affected region in Mongolia is mainly its southern part: the area of Great Lakes depression and the desert and the steppe-desert. The highest dust-storm frequency is over the three areas in the Gobi, the south side of the Altai Mountains, Ulaan-nuur Lake area and the Zamiin-Uud area. In general, it can be concluded that main source regions for Asian dust are the Gobi and the Taklamakan Desert.

Fig. 1 shows the distribution of dust-storm frequencies in the region of (60–150°E, 10–60°N). For a given station, the frequencies of the four dust-event categories, respectively denoted as f_{DIS} , f_{BD} , f_{DS} and f_{SDS} , can be estimated as follows

$$f_{DIS} = A_{DIS}/A_{obs} \quad (1)$$

etc. where A_{DIS} is the number of dust-in-suspension record and A_{obs} is the number of synoptic records. The frequency of all dust events is

$$f_{DE} = f_{DIS} + f_{BD} + f_{DS} + f_{SDS}. \quad (2)$$

Several features are observed in Fig. 1:

- (1) The Tarim Basin (Region A) is a region where dust events occur most frequently. This finding is consistent with the conclusion of Prospero et al. (2002) based on the TOMS data. The highest frequency (47%) is recorded at Hetian (80°E, 37°N);
- (2) The Gobi (Region B) is another region of frequent dust events. The highest frequency (about 15%) is recorded near the China–Mongolia border;
- (3) A belt of high dust-event frequency exists in the Hexi Corridor (Region C), stretching from northwest to southeast along the Qilian Mountains to the northeast of the Tibetan Plateau. This belt originates from the Badain Juran Desert to the north of Yumen (97°E, 40°N) in Gansu, and elongates through the Tengger Desert, passing Xi'an (109°E, 34.25°N) and ends near Xinyang (114°E, 32°N). This dusty belt reveals the profound impact of topography on the preferential route of dust transport. Almost in parallel, a second dusty belt exists to the northeast. The latter starts in Alashan Zuoqi (Inner Mongolia), passing through the Ulan Buh and the Mu Us Deserts and reaching Kaifeng (114.35°E, 34.77°N);

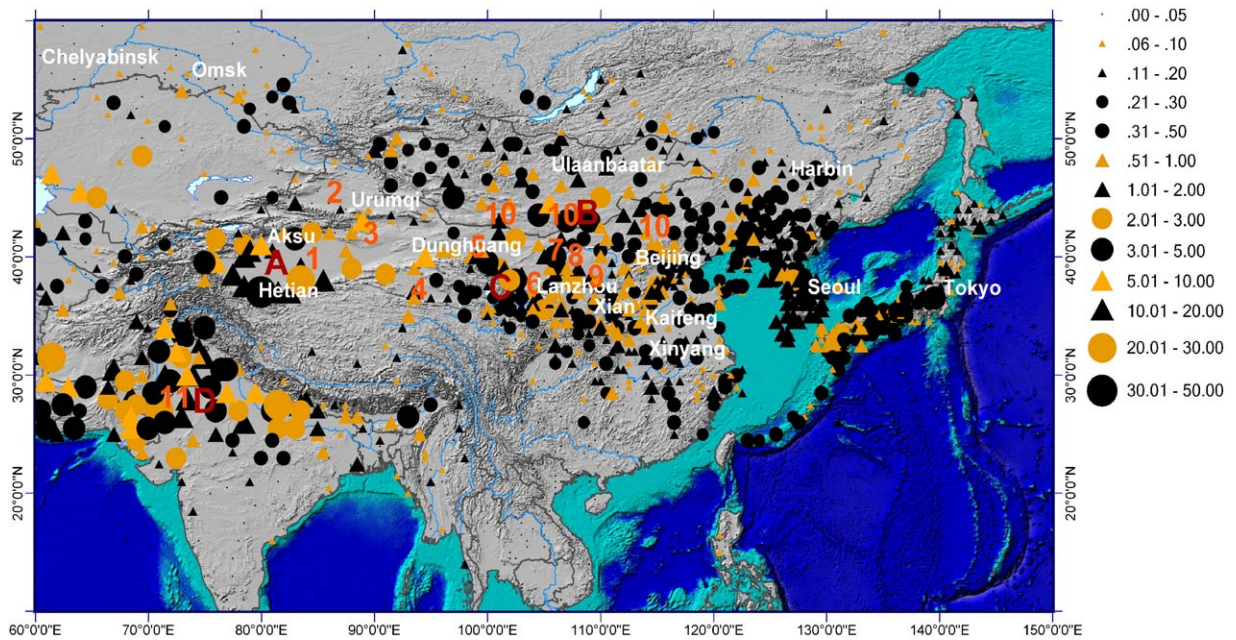


Fig. 1. Distribution of dust-event frequency, f_{DE} , derived from the meteorological records of the 5-yr period between 27 May 1998 and 26 May 2003. Main deserts in region are enumerated: 1 Taklamakan (Tarim Basin); 2 Gurbantunggut (Junggar Basin); 3 Kumutage; 4 Tsaidam Basin; 5 Badain Juran; 6 Tengger; 7 Ulan Buh; 8 Hobq; 9 Mu Us; 10 Gobi and 11 Thar. Four regions of frequent dust events, i.e., the Tarim Basin, the Hexi Corridor, the Gobi region and the Indian Subcontinent, are denoted with A, B, C and D, respectively.

(4) The northern part of the Indian Subcontinent (Region D) has high dust frequencies. The dust appears to have traveled from upstream and trapped in the region due to the blockage of the Tibetan Plateau. Some dust particles travel further along the southern boundary of the Tibetan Plateau to over the Indian Ocean and to regions much further down stream along the southwest jet stream (see also Tanaka and Chiba, 2006). Fig. 1 shows that Region D is probably the second most active area in terms of dust storm frequencies, but not much quantitative detail is known about the subcontinent dust, e.g., emission, transport, concentration etc. It is recommended that dust in this geographical area should be one of the future research focuses.

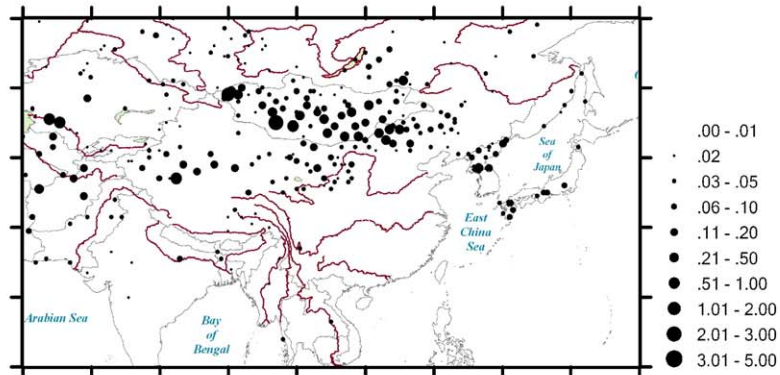
Fig. 2 offers a different perspective of Asian dust activities. Fig. 2a shows that severe dust storms occur mostly in Mongolia and Inner Mongolia, and less frequently in Hexie and Tarim Basin. Fig. 2b shows a similar picture, but more dust storms are observed in Inner Mongolia and the Tarim Basin. The prevailing synoptic system which affects the Gobi region in March, April and May is the Mongolian Cyclone. This system, associated with the East Asian trough, is often intense, leading to strong northwesterly near surface

winds, thereby generating dust storms. Dust particles from this source region are transported by the northwesterlies down stream, affecting populated areas of China, Korea and Japan. Thus, blowing-dust events occur mostly in northeastern China and dust-in-suspension events in Korea and Japan (Fig. 2c and d). The report of dust events can be subjective though, as different observers may have different preferences in reporting certain dust categories. For instance, more dust storms are reported in North Korea, which is inconsistent with the records of the nearby stations in China and South Korea. On the other hand, more dust-in-suspension episodes are reported in South Korea in comparison with the nearby stations in China, North Korea and Japan.

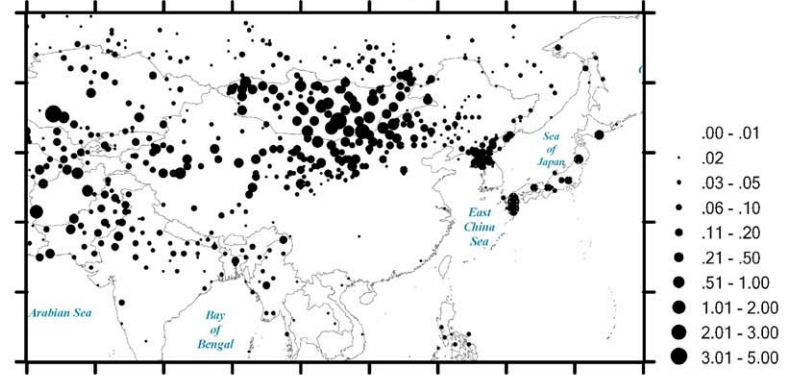
Although dust storms and severe dust storms do occur in the Tarim Basin, less intensive dust events in this region are the most frequent in Asia. A comparison of Fig. 2a,b,c and d shows that most dust events in the Tarim Basin are either blowing dust or dust-in-suspension. The main reason for this is that inside the basin, winds are much weaker than the northwesterlies over the Gobi. Likewise, dust events over the Indian Subcontinent are mostly blowing dust or dust-in-suspension.

Visibility is recorded along with the dust-event report. Although both dust and air moisture affect

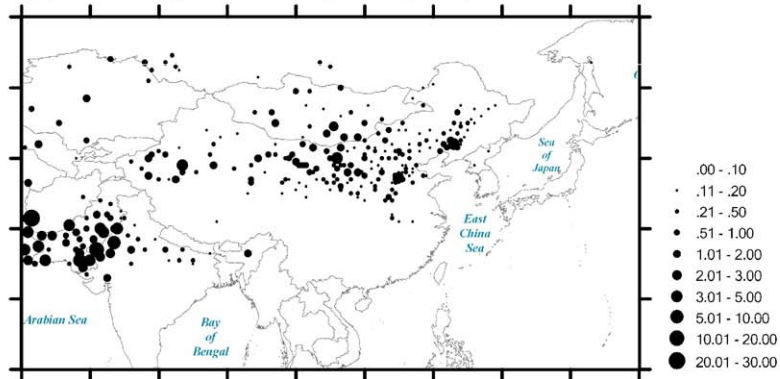
(a) Severe Dust Storm Frequency (%)



(b) Dust Storm Frequency (%)



(c) Blowing Dust Frequency (%)



(d) Dust in Suspension Frequency (%)

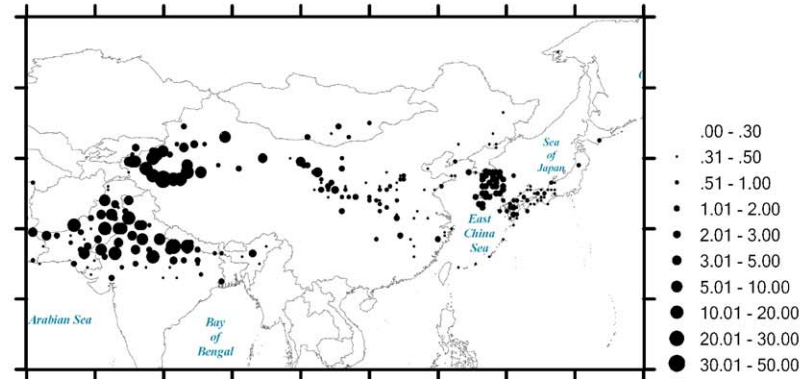


Fig. 2. Frequencies of (a) severe dust storms; (b) dust storms; (c) blowing dust and (d) dust-in-suspension.

visibility, it can be assumed that during a dust event, dust is the determining factor. Thus, dust concentration, C , can be estimated from visibility, D_v , using empirical relationships derived by fitting dust-concentration measurements to visibility. Shao et al. (2003) recommended the following empirical relationship for Asian dust

$$C = \begin{cases} 3802.29D_v^{-0.84} & D_v < 3.5 \text{ km} \\ \exp(-0.11D_v + 7.62) & D_v > 3.5 \text{ km} \end{cases} \quad (3)$$

where C is in [$\mu\text{g m}^{-3}$] and D_v in [km]. In this way, C for individual stations can be estimated from D_v . The so estimated discrete C values can then be used to generate a dust-concentration field through spatial interpolation, e.g., using an inverse-distance method.

Dust sources can be identified by combining the dust-concentration field with soil and vegetation data. Suppose a region of concern is gridded into $I \times J$ cells and $S(i, j)$ is a dimensionless indicator for potential dust source, i.e., if $S(i, j) > 0$ then cell (i, j) is a dust source. We can calculate $S(i, j)$ as follows

$$S(i, j) = C(i, j)\delta(i, j) \quad (4)$$

where $\delta(i, j) = 0$ if the following criteria are satisfied:

- (1) cell (i, j) is non-erodible, e.g, water surface, salt lakes etc.
- (2) cell (i, j) is covered by vegetation with leaf-area index exceeding L_{\min} ; and
- (3) average dust concentration for cell (i, j) , $C(i, j)$, is smaller than C_{\min} .

The estimated $S(i, j)$ for the region of (30–150°E, 5–60°N) is shown in Fig. 3. In East Asia, the Tarim Basin (Region A), the Gobi region (Region B), the Hexi Corridor region (Region C) and the Indian Subcontinent (Region D) are dust-source regions. The dust belts seen in Fig. 1 are not dust sources, but preferential routes of dust transport. What Fig. 3 shows is of course a distribution of potential dust sources in a sense of long term average. In nature, dust source regions subject to seasonal variations. For example, the Gobi region is an active dust source mainly in March, April and May, while the Tarim Basin throughout the year.

In dust prediction models to be described later, $S(i, j)$ is used to define the potential dust sources to ensure that the dust source in the numerical model is consistent with the climatic facts. However, $S(i, j)$ is not an indicator of dust-emission rate, because higher dust concentration does not always mean stronger dust emission.

2.2. Temporal variations

Dust frequency and intensity undergo variations on seasonal, annual, decadal or even longer time scales. We shall be concerned here with the seasonal to annual variations only.

2.2.1. Annual variations in source region

There is evidence to suggest that dust event frequency in Asia has been on the decline since the late 1970s until recently. In dust-affected areas of

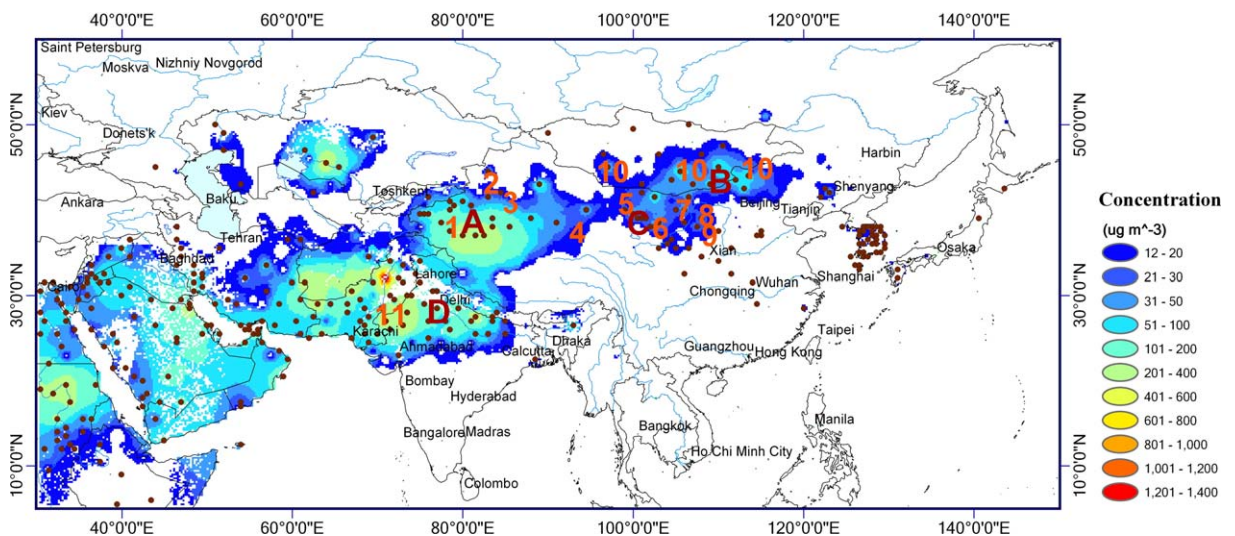


Fig. 3. Mean dust concentration (averaged over time) for the domain of analysis. Data used for this graph are derived from visibility observations from 27 May 1998 to 26 May 2003.

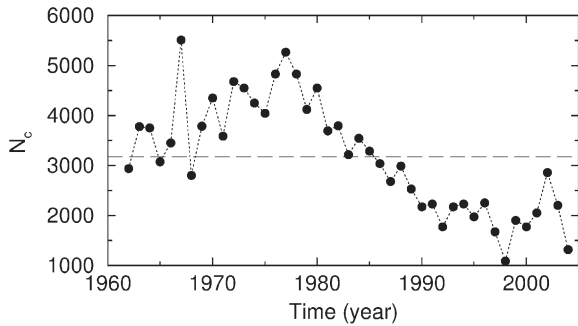


Fig. 4. Annual total number of dust days, N_c , recorded at 175 national basic meteorological stations of China for 1961–2003 (full dots with dashed line). The dashed line represents the long-term mean.

China, there exist 175 national basic meteorological stations with continuous observations since 1961. The dust variability can be studied by calculating the total number of dust days recorded at all stations, N_c . As Fig. 4 shows, in the 1960s and 1970s, N_c was high. A marked decrease in N_c occurred in the late 1970s and the 1980s, which remained below average since 1985 and reached a minimum in 1997. N_c has been increasing since 1997, but its value has not exceeded the long-term average.

2.2.2. Annual variations in transport-affected region

Kurosaki and Mikami (2003) did a similar study for Japan using the 1971–2002 synoptic data from 123 stations. Fig. 5 shows the time history of dust events observed in Japan (known as “Kosa”) that are attributed to dust transported from China. In contrast to the record of dust events in China, there is no clear time trend in Japan. We do not know why these records are so different. These differences require further study.

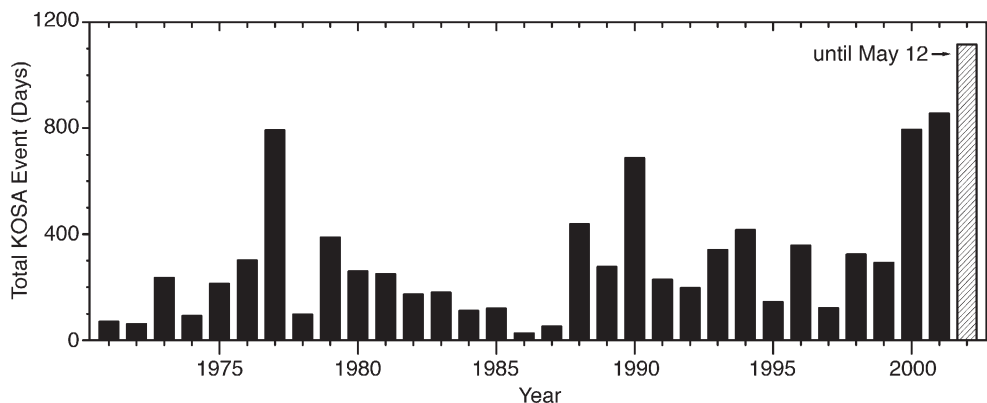


Fig. 5. Accumulative dust-event days at 123 observatories in Japan (Kurosaki and Mikami, 2003).

2.2.3. Seasonal variations in Gobi Region

Asian dust events show clear seasonal variations. Kurosaki and Mikami (2003) studied dust events in the Gobi region (88.5–131.5°E; 33.5–52.0°N) using the synoptic records of 105 stations over the period Jan 1993–Dec 2001. Fig. 6 shows the average frequencies of monthly dust events and strong winds (larger than 6.5 m s^{-1}) over the nine years. Dust events occur most frequently in spring, with the highest frequency in April. Two-thirds of the dust events occur in March, April and May. Dust events are least frequent in summer (July, August and September). The seasonal variation of dust activities is consistent with that of wind speed. Strong winds occur most frequently in spring and least frequently in summer. A weak secondary peak of strong wind frequency occurs in November; but the dust outbreak frequency has no obvious peak in this month. These results are consistent with the studies of Littmann (1991), Parungo et al. (1994) and Natsagdorj et al. (2003).

2.2.4. Tarim Basin

The seasonal variation of dust activities in the Tarim Basin differs from that over the Gobi and Gobi-dust affected downstream areas (Kurosaki and Mikami, 2005). Blowing-dust and dust-in-suspension events occur throughout the year, while the dust-storm and severe dust-storms events occur most frequently in May, about one month later than over the Gobi.

2.3. Synoptic system and wind characteristics

2.3.1. Gobi Region

The synoptic systems that generate severe dust storms over the Gobi are mostly cold air outbreaks

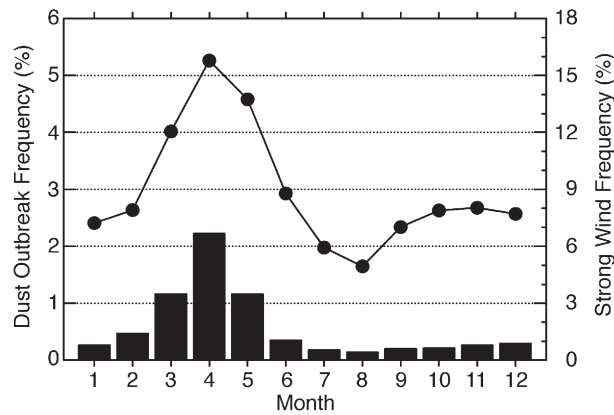


Fig. 6. Monthly dust-event frequency (bars) and strong-wind (larger than 6.5 m s^{-1}) frequency (solid line with full dots) averaged over the period of Jan 1993–Dec 2001 (Kurosaki and Mikami, 2003).

associated with intense low-pressure systems. The eastward and southeastward moving cyclones and the northwesterly wind in their cold regimes often transport large amount of dust to the eastern parts of China, Korea and Japan. Shao and Wang (2003) found that winds are very strong during dust events, mostly between 8 and 18 m s^{-1} .

2.3.2. Tarim Basin

Winds are generally weak in the Tarim Basin, but dust events are very frequent. Dust emission in the Tarim basin is likely caused by four mechanisms: (a) strong northeasterly airflow from the eastern inlet, affecting the eastern and southeastern parts of the basin; (b) strong northerly airflow climbing over the Tian Mountains, affecting the northern parts of the basin; (c) local winds, e.g., mountain–valley breeze, in isolated areas and (d) convective systems, such as dust devils.

The Tarim Basin is very dry; the annual precipitation for its southern part is as low as 20 mm; 77% of the total rain falls between June and September. The dryness is accompanied by a lack of vegetation. As a result, the threshold wind speed for dust emission in the Tarim is small (around 4 m s^{-1}) in comparison to that for the Gobi (around 7 m s^{-1}). The Tarim Basin is almost completely surrounded by high (several thousand meters) mountains. The only low-altitude opening to the basin is in the eastern end and it is quite narrow. This geographic setting ensures that gentle winds prevail within the basin. However, strong northeasterly winds may occur in the eastern and southeastern part of the basin, sufficiently strong to generate dust storms. The flows from the eastern and

northern parts converge to the southern part of the Tarim. The circulation in the basin creates favorable conditions for dust to remain suspended for a long time and the export of dust from the basin may not be as large as commonly believed. It seems that although the Tarim Basin is a region of high dust concentration, it may not be a region of strong dust provision for the global atmosphere. Dust emitted from the basin may deposit back into the basin. This is in contrast to the Gobi where dust entrained into the atmosphere is advected downstream. Thus, although the mean dust concentration over the Gobi is somewhat smaller, it may still be a stronger dust source than the Tarim Basin.

2.3.3. Hexi corridor

Dust weather in Hexi corridor is often caused by intense frontal systems. As an example, the system that generated the 5 May 1993 extreme dust storm is depicted in Fig. 7. A combination of large-scale weather pattern and topological effects led to the development of the intense frontal system. On 2 May 1993, cold air was gathering strength in north Siberia and a trough was located near Omsk in West Siberian Plain. As the trough deepened, the northwesterly wind behind the trough increased. By 5 May 1993, a cutoff low was developing, accompanied by a cold airburst southeastwards. The blockage of the Altai and Tian Mountains generated a channel effect that strongly accelerated the near surface wind. At the same time, the adiabatic heating from the Tibetan Plateau to the south strengthened the north–south temperature contrast, which also increased the flow speed. The near surface wind for this event reached 35 m s^{-1} .

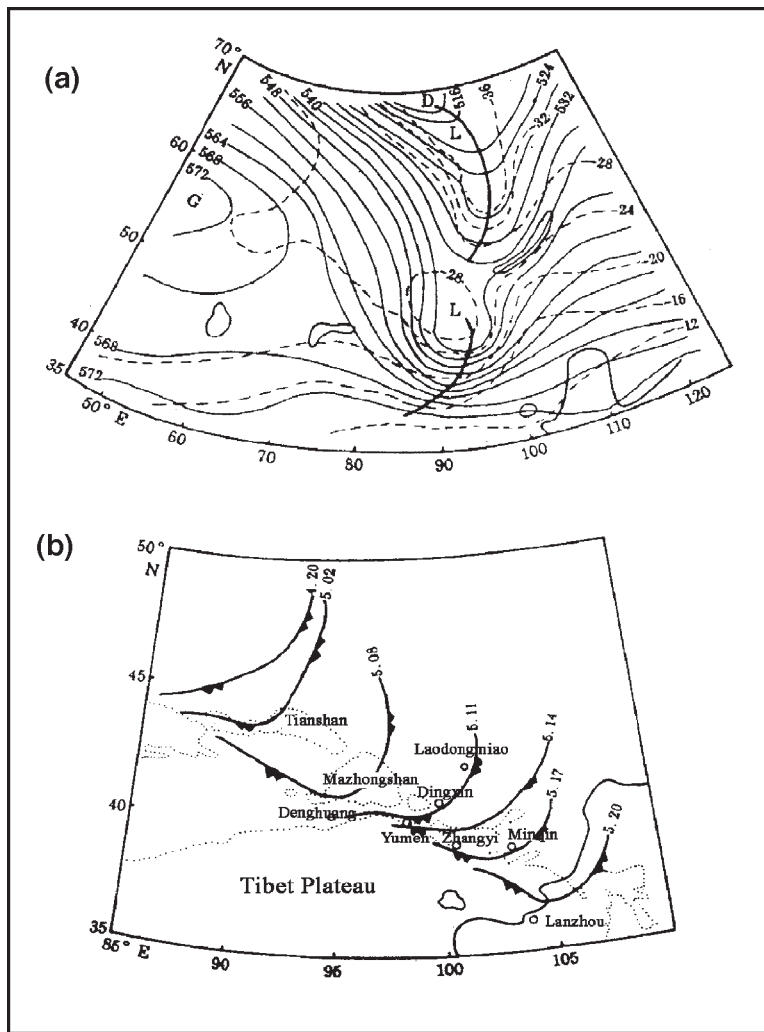
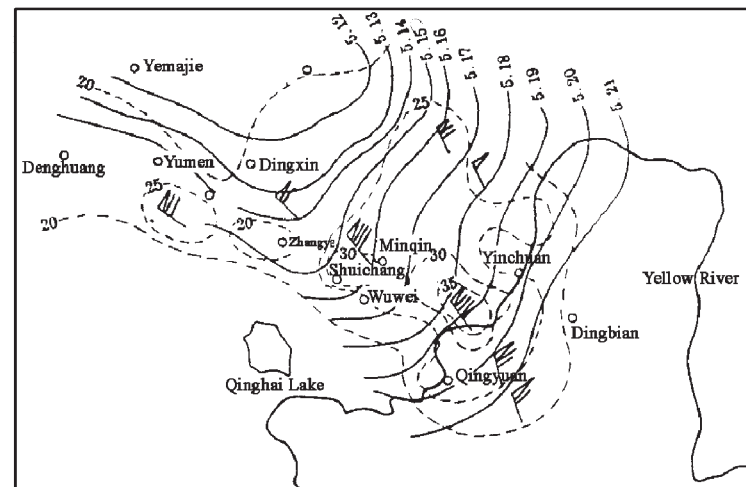


Fig. 7. Synoptic situation for the 5 May 1993 severe dust storm in northwest China. The development of the cutoff low can be clearly seen from the 500 hPa weather map, which is accompanied by a cold air burst towards southeast. The movement of the surface cold front is also shown. Synoptic situation (surface weather) map for the 5 May 1993 severe dust storm (Wang et al., 1995).



3. Integrated dust storm modelling and monitoring system

Efforts have been made to develop integrated dust modelling systems which couple models for atmospheric, land-surface and aeolian processes, real-time dust observations and databases for land-surface parameters, so that the dust-storm dynamics and the environmental control factors are adequately represented (Shao, 2000). Fig. 8 shows a possible framework. The system consists of the modeling, monitoring, database and data-assimilation component. The modeling component comprises an atmospheric model and modules for land-surface processes, dust emission, transport and deposition. The atmospheric model, either global, regional or meso-scale, serves as a host for the other modules. Most atmospheric models have advanced numerics for atmospheric dynamics and physical processes, e.g., radiation, clouds, convection, turbulent diffusion etc. A land-surface scheme simulates the energy, momentum and mass exchanges between the atmosphere, soil and vegetation. For dust modeling, it produces friction velocity and soil moisture as outputs. The dust emission scheme obtains friction velocity and soil moisture from the land-surface scheme and other spatially distributed parameters from the GIS database, and calculates dust-emission rates for different particle-

size groups. To predict dust motion, the transport and deposition model obtains wind, turbulence and precipitation data from the atmospheric model, and dust-emission rate and particle-size information from the dust-emission model.

Land-surface data are required for the atmospheric model as well as for land-surface, dust-emission and dust-deposition schemes. The key land-surface data required for dust modeling include:

- (1) soil particle-size distribution
- (2) soil surface characteristics
- (3) vegetation coverage
- (4) vegetation leaf-area index and roughness frontal area index.

Soil particle-size data are of critical importance. For large-scale dust modeling, one approach is to classify soils according to the USDA (the United States Department of Agriculture) soil texture triangle. This has two advantages: (1) the soil classifications for the dust-emission and land-surface schemes are consistent; (2) soil particle-size data can be collected at different locations over the world and the data organized according to this classification for establishing a soil particle-size database. Soil particle-size distribution, $p(d)$ (d is particle diameter), can be regarded as a

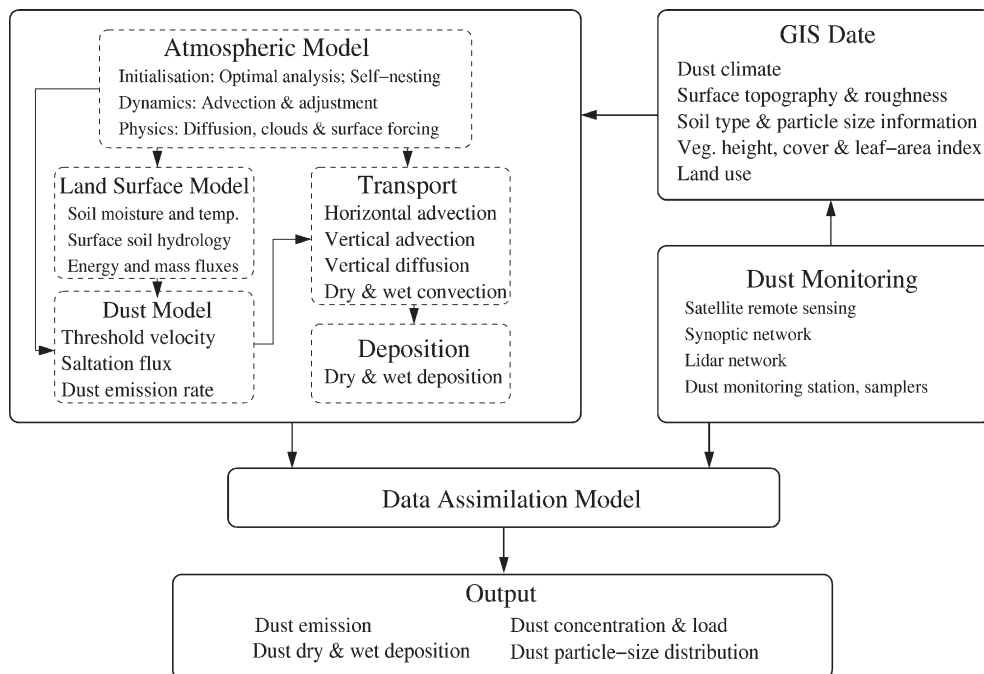


Fig. 8. Framework of an integrated dust modelling and monitoring system.

composite of several lognormal distributions (Gomes et al., 1990; Chatenet et al., 1996)

$$p(d) = \frac{1}{d} \sum_{j=1}^J \frac{w_j}{\sqrt{2\pi}\sigma_j} \exp\left(-\frac{(\ln d - \ln D_j)^2}{2\sigma_j^2}\right) \quad (5)$$

where J is the number of modes, w_j is the weight for the j th mode of the particle-size distribution, D_j and σ_j are the parameters for the lognormal distribution of the j th mode. The parameters are obtained by fitting Eq. (5) to data of particle-size distribution measurements. The soil particle-size database is then made of data of J , w_j , σ_j and D_j .

The calculation of wind-erosion threshold friction velocity requires the frontal area index of roughness elements λ (or aerodynamic roughness length z_0) and soil moisture w as inputs. The former is slowly varying with time and can be assumed constant for individual dust events. Soil moisture experiences both diurnal and seasonal variations, responding to precipitation and evaporation. For vegetated surface, λ can be derived from a combination of satellite NDVI (Normalized Differential Vegetation Index) and vegetation-type data. In practice, empirical relationships between λ and NDVI are assumed for different vegetation types.

Another component of the integrated system is dust monitoring using both conventional and modern technologies. Satellites can now provide continuous dust monitoring over large areas and the developments of inverse data calculation methods are producing quantitative estimates of dust load. Networks of lidar have been under establishment, which provide dust profile estimate at a number of locations. Further, stations equipped with dust samplers are set up. These various data provide a valuable source of data for data assimilation of dust storms and for model validation.

Since the later 1980s, models for global, regional and local dust problems have been developed. Early attempts on dust modeling were made by Westphal et al. (1988), Gillette and Hanson (1989) and Joussaume (1990). Examples of global dust models include the studies of Tegen and Fung (1994), Ginoux et al. (2001, 2004), Zender et al. (2003) and Tanaka et al. (2003). Examples of regional dust models include the studies of Shao and Leslie (1997), Wang et al. (2000), Nickovic et al. (2001), Uno et al. (2001), Gong et al. (2003) and Liu et al. (2003). Seino et al. (2005) simulated dust storms in the Tarim Basin using a meso-scale dust model, and Uno et al. (2005) applied multi-nesting techniques to modeling dust activities in the Tarim Basin. Shao et al. (2003) applied an integrated system to real-time dust-storm

prediction. A summary of some of the systems is given in Table 1.

3.1. Dust-emission schemes

The estimate of dust-emission rate on large scales relies on dust-emission parameterization schemes. Zender et al. (2003) suggested that dust-emission schemes can be divided into three categories according to scheme complexity, namely, simple, intermediate and complex. This classification is useful (but debatable). To facilitate description, we classify dust-emission schemes into the categories of α , β and γ .

In α -schemes, the dust-emission rate, F , is parameterized in terms of the power of wind speed or friction velocity, and then an empirical particle-size distribution is imposed on F to obtain dust emission rates for different particle sizes (Tegen and Fung, 1994; Mahowald et al., 1999, 2003; Perlwitz et al., 2001). The α -schemes can be formulated as follows:

$$F = \alpha_u (u_*^n - u_{*t}^n) \quad (6)$$

$$\tilde{F}(d_j) = P(d_j)F \quad (7)$$

where u_* is friction velocity, u_{*t} is threshold friction velocity, $\tilde{F}(d_j)$ is the dust emission rate and $P(d_j)$ the dust-mass fraction of j th particle-size bin. The coefficient α_u is empirical, in which various wind-erosion factors are embedded. The $F \sim u_*^n$ relationship is first proposed by Gillette and Passi (1988). Field observations suggest that this relationship is not unreasonable and n is in the range of 3 to 5 (Nickling et al., 1999). The formulation of α -schemes is simple, but it is not simple to estimate α_u , u_{*t} and $P(d)$ in practice. It is not clear how u_{*t} should be interpreted in (6).

The β -schemes have been used in global dust modeling (Ginoux et al., 2001; Woodward, 2001). Differences exist in details among the β -schemes reported in the literature, but a common feature is that in these schemes, simplified wind-erosion physics is considered, supplemented with dust climate data derived from satellite observations. We use the scheme of Zender et al. (2003) as an example to illustrate this approach. The scheme is built around the argument that dust emission is proportional to saltation (Shao et al., 1993; Alfaro and Gomes, 2001) and takes into consideration of various factors influencing dust emission. The dust-emission rate for the j th particle-size group, F_j is parameterized as

$$F_j = T \cdot A_m \cdot S \cdot \alpha_s \cdot Q_s \sum_{i=1}^I M_{ij} \quad (8)$$

Table 1
A summary of dust modeling systems. The reference abbreviations are: DT94 (DeFries and Townshend, 1994); G86 (Giogi, 1986); GC86 (Giorgi and Chameides, 1986); MB95 (Martcorena and Bergametti, 1995); PI03 and IP03 (Park and In, 2003; In and Park, 2003); R92 (Raupach, 1992); S88 (Stull, 1988); SP98 (Seinfeld and Pandis, 1998); W85 and W89 (Wesely et al., 1985; Wesely, 1989); Z01 (Zhang et al., 2001)

Model name	CEMSYS5	CFORS	COAMPS	DEAD	DREAM	GOCART	ITR	HCM	MASINGAR	NRL	NARCM
Atmospheric model	Regional, HIRES	Regional, RAMS	Regional, COAMPS	Embeddable, Global	Regional, NCEP-Eta	Global, NASA GEOS-DAS reanalysis	Global, TM3 or ECHAM5 and regional LM-MUSCAT	Regional, RDAPS	GCM, JMA98	GCM, NOGAPS	Regional, RCM
Dust scheme	γ -scheme,	α -scheme, $F \sim u_*^4$	α -scheme, $F \sim u_*^4$	β -scheme	γ -scheme	β -scheme	α -scheme $F \sim u_*^3$	α -scheme, $F \sim u_*^4$	γ -scheme	α -scheme, $F \sim u_*^4$	α -scheme, $F \sim u_*^3$
Size range (μm)	<40	0.2–40	0.05–36	<20	1.46–76	0.2–6	0.2–100	0.2–74	0.2–20	<40	0.1–41
Dust bins	6	12	10	4,	4	4	7	11	10	1	12
PSD treatment	Model, depends on wind speed and parent soil PSD	Specified, linear to d for $d < 1 \mu\text{m}$; to $\log d$ for $d > 2 \mu\text{m}$	Specified, bimodal lognormal size	Specified, sectional in $\log d$ with prescribed sub-bin distribution	Specified	Specified linear within each bins	Specified, depends on wind speed and parent soil PSD	Specified, log normal	Model, depends on wind speed and parent soil PSD	Specified	Specified, linear to $\log d$ for $0.25 < d < 16 \mu\text{m}$, to d otherwise
Snow cover	Land-surface model	Observation, monthly averaged	USGS landuse 1-km database	Model output	None	Reanalysis	Model output	None	Land-surface model	Model output	Observation, monthly averaged
Soil moisture	Land-surface model	Land-surface model	None	Land-surface model	Land-surface model	Re-analysis	Land surface model	None	Land-surface model	Land-surface model	Land-surface model
Drag partition	R92	None	None	MB95	None	None	None	None	R92	None	MB95
Vegetation treatment	u_{*c} a function of NDVI; dust emission reduced	u_{*c} a function of NDVI	USGS landuse database	Reduces fraction of erodible ground	None	None	Source area function of seasonal FPAR and vegetation type	Dust emission reduced	Dust emission reduced	Static field with seasonal dependence	u_{*c} a function of vegetation
Land use	Merged USGS and LREIS soil data	USGS vegetation data	USGS landuse data	Provided by host model	USGS vegetation data	AVHRR	RIVM land use data	USGS vegetation data	DT94	NCAR 1-degree database	USGS vegetation data and Chinese desert map
Soil texture	USDA soil texture class; Minimally and fully dispersed PSD	FAO soil texture data	None	IGBP-DIS soil texture	FAO soil texture data	None	FAO soil texture data	PI03, IP03	ORNL soil data	None	Soil texture map
Roughness length	HIRES default and estimates from NDVI	RAMS default	USGS landuse database	Globally uniform over erodible surfaces	NCEP/ETA default	Re-analysis	ERS SAR	Pi03, IP03	MASINGAR default	USGS database, seasonal variation	Estimates from roughness element density and height
Dry deposition	Gravitational settling and diffusion	Constant value	Function of wind stress, S88	Gravitational settling and diffusion	G86 dry deposition scheme	Gravitational settling and diffusion	Gravitational settling and diffusion	W85, W89 method	Resistance model, SP98	Gravitational settling and diffusion	Z01 resistance approach size dependent.
Wet deposition	Below cloud scavenging	Scavenging ratio method	Scavenging ratio method	In-, below-cloud scavenging	Scavenging ratio method	In- and below cloud scavenging	Scavenging ratio, below-cloud	RADM	GC86	Scavenging ratio method	In- and below cloud scavenging
Cunningham Correction	No	No	Yes	Yes	No	Yes	Yes	No	Yes	No	Yes
References	Shao (2001, 2004)	Uno et al. (2003)	Liu et al. (2003)	Zender et al. (2003)	Nickovic et al. (2001)	Ginoux et al. (2001, 2004)	Tegen et al. (2002, 2004)	In and Park (2003)	Tanaka et al. (2003)	Christensen (1997)	Gong et al. (2003)

where $I=3$ is the number of modes; $M_{i,j}$ is the mass fraction of particle size bin j and mode i ; T is a global tuning factor selected to produce a reasonable climatological simulation, e.g., $T=7 \times 10^{-4}$ would result in a global dust emission of 1500 Tg yr^{-1} ($d < 10 \mu\text{m}$) in the study of Zender et al. (2003). A_m is the fraction of erodible surface; α_s is the saltation bombardment efficiency (Marticorena and Bergametti, 1995); Q_s is streamwise saltation flux (White, 1979); and S is the source erodibility factor. The advantage of the scheme is that observed data, in particular satellite data, are used to constrain the scheme behavior by tuning T and S . However, there are two main problems associated with this approach. (1) The tuning of T and S requires the global dust emission to be known, but this is not the case. In practice, the global dust emission, i.e., the integral of F_j over the globe, is assumed to be such that the model estimated global dust load is in some sort of agreement with the inversely-calculated global dust load from satellite remote sensing. Unfortunately, the latter has very large uncertainties. For example, the inverse calculation of dust load depends on dust optical depth which is closely linked to the fine-particle (less than 1 μm diameter) concentration, while dust load is largely dependent on the surmicron particle concentration. (2) Global dust load is determined not only by dust emission, but also by dust deposition. Very little is known about the global dust deposition. Thus, the dust emission estimates using Eq. (8) are not independent from the uncertainties in dust deposition estimates.

The γ -schemes are spectral dust-emission schemes based on wind-erosion physics. Taking into consideration of the three dust emission mechanisms (aerodynamic entrainment, saltation bombardment and aggregates disintegration), Shao (2001, 2004) suggested that

$$\tilde{F}(d_i, d_s) = c_y \eta_{fi} [(1-\gamma) + \gamma \sigma_p] (1 + \sigma_m) \frac{gQ}{u_*^2} \quad (9)$$

where \tilde{F} is the dust emission rate for the i th size particle group generated by the saltation of particles of size d_s , c_y is a dimensionless coefficient and γ is a weighting function which satisfies

$$\gamma = \begin{cases} 1 & u_* \rightarrow u_{*t} \\ 0 & u_* \rightarrow \infty \end{cases} \quad (10)$$

Q is the streamwise saltation flux of d_s ; g is acceleration due to gravity; $\sigma_p = p_m(d_i)/p_f(d_i)$ with $p_m(d_i)$ and $p_f(d_i)$ being the minimally- and fully-dispersed

particle size distribution. The bombardment efficiency σ_m is estimated by

$$\sigma_m = 12u_*^2 \frac{\rho_b}{p} \left(1 + 14u_* \sqrt{\frac{\rho_b}{p}} \right) \quad (11)$$

where ρ_b is soil bulk density and p is soil plastic pressure.

This is a spectral model, because the rate of dust emission for any particle size bin is determined by

$$\hat{F}(d_i) = \int_{d_1}^{d_2} F(d_i, d) \delta d. \quad (12)$$

where d_1 and d_2 are the lower and upper limit of saltation particle size. The total dust emission rate is

$$F = \sum_{i=1}^{i=I} \hat{F}(d_i) \quad (13)$$

with I being the number of dust size bins. Shao (2004) compared the predicted F using the scheme with observed data for several soil texture and surface conditions. The scheme is sufficiently general and has the capacity to predict dust emission rate from various soils. It is found that c_y falls between 10^{-5} and 5×10^{-5} and p falls between 1000 and 50,000 Pa.

The increased understanding of wind-erosion physics has enabled the development of dust-emission schemes on a firmer footing. However, the accuracy of the dust-emission schemes is limited by the lack of capacity in specifying the temporal and spatial variations of model parameters. This is a problem for all dust schemes. In summary, we provide the following comments:

- (1) α -schemes: The α -schemes are simple in formulation; there is evidence that $F \sim u_*^n$ is not unreasonable; The parameter α_u in Eq. (6) is empirical; there are no guidelines for its specification; There is confusion in literature regarding the interpretation of u_{*t} in α -schemes: it is sometimes interpreted as the threshold friction velocity of the surface and sometimes as that of dust particles. The former is more reasonable; The α -schemes are not spectral schemes. Eq. (7) requires the specification of $P(d)$ which is unknown.
- (2) β -schemes: Dust-emission physics of the β -schemes can be similar to that of either the α - or the γ -schemes; It is advantageous of using satellite data to modify the estimated dust emission rate. However, it is difficult to infer dust emission rate from satellite data, as discussed earlier.

- (3) γ -schemes: In γ -schemes, the current understanding of wind-erosion physics has been taken into account; they are more complex than the α -schemes, but are still very simple; The input parameters required by the γ -schemes have clear physical interpretations; The γ -schemes require soil and land-surface data that are not yet widely available, in particular the soil plastic pressure and parent soil particle size distributions.

Dust emission mechanisms require further investigation. Based on field experience in the Tarim Basin, M. Mikami (personal communication) suggested that dust devils are important to dust emission. The difficulty in achieving the accuracy of dust emission schemes is exacerbated because dust emission can vary by several orders of magnitude (Shao, 2004). A major problem facing the dust modelling community is the lack of direct dust flux data for model validation. This is in particular the case for the Asian dust source regions. Additional discussions on dust emission modeling are given in Section 5.

3.2. Dust model applications

Dust models have a wide range of applications, the most important ones are

- (1) dust storm prediction;
- (2) understanding of dust processes;
- (3) quantification of global dust cycle; and
- (4) re-constructing past climates.

Dust models have been applied to the prediction of Asian dust storms with considerable success. Several research groups have reported that their dust models can correctly predict the spatial pattern and temporal evolution of Asian dust storms, as well as the order of magnitude of dust concentration, emission and deposition (e.g., Gong et al., 2003; Shao et al., 2003; Han et al., 2004). As an example, Fig. 9 shows the 24-h forecasts of near-surface dust concentration using CEMSYS5 (Shao et al., 2003). For detailed validation of the model results has been presented in the latter paper and is therefore not repeated here.

In Fig. 9, the predicted near-surface dust concentrations for March 19, 20, 21 and 22 are shown together with the dust concentration derived from visibility data using Eq. (3). The predictions and the observations agree well in spatial pattern and intensity. The dust episode first developed on 19 March over the Gobi near the China–Mongolia border. Near the center

of the dust storm [about (105°E, 42°N)], the predicted and the observed near-surface dust concentration exceeded 10,000 $\mu\text{g m}^{-3}$. In the next two days, the center of the dust storm moved eastward and dust was widespread, but the near-surface dust concentration was decreasing. By 21 March, dust clouds covered a large part of China, Korea and the dust front reached Japan. By 22 March, both model prediction and observation showed a dust band stretching several thousands of kilometers.

Dust models have been used to studying dust processes (e.g., Seino et al., 2005; Jung et al., 2005). Uno et al. (2005) applied the CFORS model to examining the characteristics of dust transport in the Tarim Basin. They ran the model with three resolutions (81, 27 and 9 km) for April 2001 and examined the model performance against the synoptic records and the ADEC observations (Mikami et al., 2002). Their model was able to reproduce the complex flow patterns in the Tarim Basin for dust storm generation, e.g., the strong down slope wind from the Tianshan Mountains and the strong easterly flow from the Hexi Corridor. A strong easterly flow of 2 km thick was found to be prevalent over an area of 400 km (north–south) by 1000 km (east–west). A high dust concentration layer, approximately 1500 m thick, was found in the convergent zone of the cold airflow. The dust was then transported further westwards.

Based on dust-model output, dust-budget terms, including dust emission, dust deposition and dust load can be estimated. The simulation of Shao et al. (2003) for the period of 1 March to 30 April 2002 suggests that the maximum dust-emission rate associated with individual dust storms in the Gobi region is around 5000 $\mu\text{g m}^{-2} \text{s}^{-1}$. The maximum dust emission rate predicted by Park and In (2003) is around 12,000 $\mu\text{g m}^{-2} \text{s}^{-1}$ and that by Han et al. (2004) is around 3500 $\mu\text{g m}^{-2} \text{s}^{-1}$.

The cumulative net dust flux for a simulation period T can be estimated as follows

$$F_{\text{net}} = \int_0^T (F-D)dt \quad (14)$$

where F and D are dust emission and deposition, respectively. Based on the simulation over March and April 2002, Shao et al. (2003) found that the regions of net positive dust flux (source) are mainly the deserts in China and southern Mongolia. The Gobi Desert has the strongest net dust emission, reaching 1000 t km^{-2} over the March–April period (corresponding to a flux of around 190 $\mu\text{g m}^{-2} \text{s}^{-1}$). Zhao et al. (2003) and Han et al. (2004) also studied dust budget for the Gobi region, but

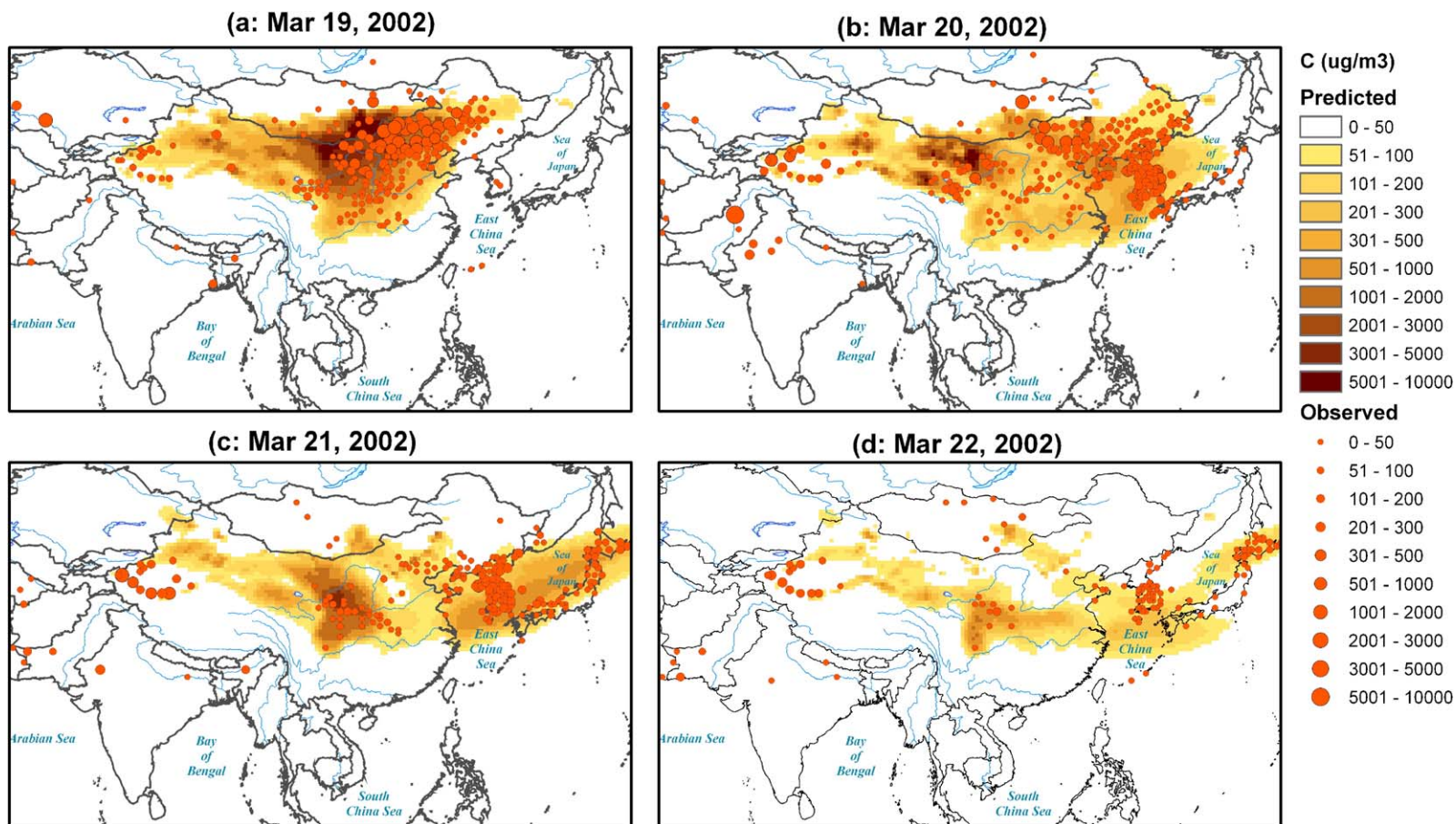


Fig. 9. Comparisons of the predicted and observed near surface dust concentration (in $\mu\text{g m}^{-3}$) for four days from 19 to 22 March 2002. The model results are the 24 h forecasts using CEMSYS5.

the results are difficult to compare due to the different methods of computation.

Net negative dust flux (sink) covers a wide area. Large parts of China, Korea and Japan receive net deposition. The magnitude of net deposition reaches up to $2.6 \times 10^5 \text{ kg km}^{-2}$ in the two month period of March and April 2002. The Loess Plateau, situated immediately downstream of the Gobi, is the strongest dust sink, receiving about $5.0 \times 10^4 \text{ kg km}^{-2} \text{ mon}^{-1}$ (in peak dust season). Gao et al. (1997) reported that (dry) dust depositions in Xi'an (109°E , 34°N), Lanzhou (104°E , 36°N) and Baotou (110°E , 41°N) are 19, 35 and $32 \text{ g m}^{-2} \text{ mon}^{-1}$, respectively, corresponding to 1.9, 3.5 and $3.2 \times 10^4 \text{ kg km}^{-2} \text{ mon}^{-1}$, consistent with the predicted dust deposition in order of magnitude. A deposition zone also exists along the southern fringes of the Tibet Plateau. Dust deposited to this area has an origin located to the southwest of the Tibet Plateau, possibly northwestern India, Pakistan, Afghanistan etc.

During peak dust season, the estimated dust load reaches up to $1.7 \times 10^3 \text{ kg km}^{-2}$. A high dust load zone exists along the northern border of the Tibet Plateau. In the west, the high dust load zone is divided by the Tian Mountains into two horns, one stretching into the Talimu Basin and the other into the Zhunge'er Basin. In the east, the high dust load zone diverges downstream of the dust source region. On the basis of the numerical simulations for March and April 2002, the range of total dust emission, total dust deposition and total dust load for the Asian region are for the East Asian region are shown in Table 2.

The orders of magnitude of these dust budget terms are comparable with those of Han et al. (2004). However, again the values are difficult to compare directly, because the simulation areas are different.

4. Satellite remote sensing

Satellite remote sensing is advantageous in monitoring the significant variations of dust storms in space and time (Husar et al., 2001). Sensors on polar orbiting

and geostationary satellites detect radiances of various surfaces of the Earth through different spectral channels. The channels are set in correspondence to the atmospheric radiation windows and water vapour absorption band. The main channels are VL (visible light, $0.65\text{--}0.85 \mu\text{m}$), NIR (near infrared, $1.6 \mu\text{m}$), MIR (middle infrared, $3.7 \mu\text{m}$), WV (water vapor, $6.7 \mu\text{m}$) and TIR (thermal infrared, 11 and $12 \mu\text{m}$). In terms of dust storm monitoring, the main challenges are to combine the various satellite remote sensing signals

- (1) to provide real-time monitoring through dust storm identification from satellite imagery;
- (2) to derive land-surface and atmospheric parameters for dust modeling;
- (3) to derive physical quantities for validation of dust predictions and for data assimilation; and
- (4) to derive long-term dust climatology.

4.1. Dust storm monitoring

The task of dust storm monitoring is to identify dust clouds from satellite imagery. This is done on the basis of the radiation and scattering characteristics of dust particles. During Asian dust storms, dust particle size may vary between 0.01 and $100 \mu\text{m}$. Techniques have been under development since the 1970s for dust identification from VIR (visible and near-infrared) (Griggs, 1975; Carlson, 1979; Norton et al., 1980) and TIR images (Shenk and Curran, 1974; Ackerman, 1989). The TIR method has the advantage of being able to detect dust over high albedo surfaces and in nighttime. However, it is often the case that the behavior of dust, ground surface and cloud are similar for a specific channel (e.g., VIS and TIR), and it is difficult to identify dust from these other radiating bodies using a single channel. A combination of signals from various channels is more effective.

4.1.1. Dust signal from 1.06, 3.75 and 11 μm signals

It has been found that a statistical relationship exists between the $1.06 \mu\text{m}$ reflectance, $R_{1.06}$, and the 3.75 and $11.0 \mu\text{m}$ brightness temperature ratio

$$R_{1.06} = a(T_{3.75}/T_{11}) + b \quad (15)$$

where a and b are empirical coefficients and $T_{3.75}$ and T_{11} are respectively the 3.75 and $11.0 \mu\text{m}$ brightness temperature (Zheng et al., 2001). A scatter plot of $R_{1.06}$ against $T_{3.75}/T_{11}$ allows the identification of dust from ground surface, low clouds and high clouds.

Table 2

Order of magnitude of total dust emission, dust deposition and dust load over Asia. The values are based on numerical simulations Shao et al. (2003) for March and April 2002, a very active dust season

	Min	Max
Total dust emission (10^6 kg day^{-1})	11.5	65.7
Total dust deposition (10^6 kg day^{-1})	10.8	51.4
Total dust load (10^6 kg)	5.5	15.9

4.1.2. Dust signal from 1.6 μm

For 1.6 μm signals, dust-particle size is similar to the signal wavelength, and the Mie-diffusion theory is applicable. Air molecules and fine aerosols have a negligible effect on the signals. The 1.6 μm signal and the intensity of dust event have a linear relationship and is thus applicable to dust recognition.

4.1.3. Dust signal from TIR signals

In the 10.5–12.5 μm spectral range, dust particles, aquatic particles and aerosol behave differently in radiation absorption and emission. Atmospheric composition can be estimated on the basis of the differences. The radiance observed by satellite, I_λ , can be expressed as

$$T_\lambda \approx B_\lambda(T_s) \cdot \exp(-\tau_\lambda) + [1 - \exp(-\tau_\lambda)] \cdot R_\lambda(T_a) \quad (16)$$

where B_λ is the Planck function, T_s and T_a are respectively surface temperature and effective air temperature, τ_λ is aerosol optical thickness. Eq. (16) shows that I_λ is made of two components: one is the infrared radiation from the surface and the other the infrared radiation of the atmosphere. For small τ_λ , $I_\lambda \approx B_\lambda(T_s)$; for large τ_λ , $I_\lambda \approx B_\lambda(T_a)$. It is now conventional to split the 10.5–12.5 μm spectral range into two channels, the 11 μm channel and the 12 μm channel. The decays of the 11 and 12 μm signals due to the absorption of dry dust are different: the former decays somewhat stronger than the latter. As a result, the 12 μm signal sensed by satellite is stronger than the 11 μm signal. Let T_{12} and T_{11} denote the 12 and 11 μm brightness temperatures, respectively, $\bar{T} = (T_{12} + T_{11})/2$ the average brightness temperature and $\Delta T = T_{12} - T_{11}$ the brightness temperature difference. Tests show that areas with $\Delta T \geq 1$ K and $\bar{T} < 290$ K represent dust. Although dust and cirrus clouds have similar ΔT , they are very different in \bar{T} because cirrus clouds (c. a. 8 km) are much higher than dust clouds (c.a. 3 km).

In practice, a combination of the above-described techniques is used for dust storm monitoring. A possible procedure is as follows:

- (1) Cirrus and dust: Cirrus clouds made of icy particles are semi-transparent and the cloud-top temperatures are low. Using the Planck non-linear theory, the presence of cirrus clouds can be identified from the fact that \bar{T} is low and ΔT is positive. For dust clouds, we also have $\Delta T \geq 0$, but \bar{T} is much higher.

- (2) Low-level clouds and dust: Low-level clouds (including fog) and dust have similar \bar{T} and ΔT . However, in contrast to dust, low-level clouds are made of water droplets, their optical thicknesses are large and are highly reflective to the 0.65–0.85 μm light. The VIS reflectance can be used for low-level cloud identification.
- (3) Ground surface and dust: Ground surface and dust have similar reflectance to visible light, but have differences in the $T_{3.75}/T_{11}$ ratio or ΔT . Based on these differences, dust clouds can be separated from ground surface.
- (4) Dust signal at 1.6 μm : In case of strong dust storms, large quantities of giant particles (several microns) exist in dust clouds, which are highly reflective to the 1.6 μm radiation in comparison to clouds and ground surface. The 1.6 μm signal is very useful for the identification of severe dust storms.

As an example, Fig. 10 shows the MODIS image of the 10 March 2006 dust-storm. MODIS (Moderate Resolution Imaging Spectroradiometer) is a key instrument aboard the Terra (EOS AM) and Aqua (EOS PM) satellites. Terra MODIS and Aqua MODIS are viewing the entire Earth's surface every 1 to 2 days, acquiring data in 36 spectral bands between 0.4 and 14 μm . The

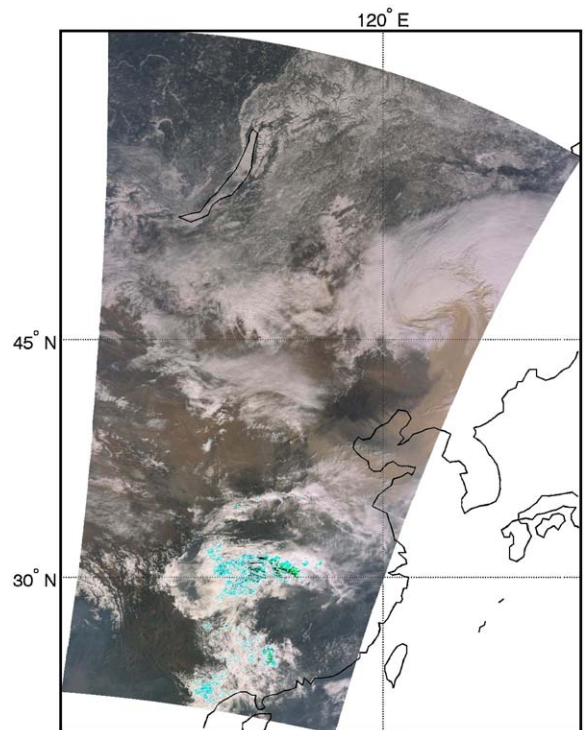


Fig. 10. MODIS image of the 10 March 2006 dust storm.

MODIS data has three resolutions of 250, 500 and 1000 m.

4.2. Dust storm intensity index

Some progress has also been made to give qualitative estimates of dust storm intensity from satellite remote sensing. A dust storm intensity index can be expressed as

$$I_{ds} = a \cdot [\exp(bR_{1.6}) - 1] \cdot \Delta T \quad (17)$$

where $R_{1.6}$ is the 1.6 μm reflectance; a (about 10) and b (about 0.8) are adjustable coefficients. This index takes the advantage of the sensitive response of the 1.6 μm signal to severe dust storms and the sensitive response of ΔT to weak dust events. Fig. 11 shows the calculated I_{ds} for the 6 April 2002 severe dust storm using the FY-1D satellite data.

4.3. Inverse calculation of dust quantities from satellite remote sensing

A major challenge in satellite remote sensing is to retrieve dust-related physical quantities, such as dust

load, M , i.e., total dust mass in an air column. Tanré et al. (1997) demonstrated that the VIR technique can be used to retrieve dust load over ocean. However, to retrieve dust load for over land is more difficult, because the signal sensed by the satellite is contaminated by land surface radiation.

Wen and Rose (1994) developed an algorithm for the retrieval of particle size, optical thickness and aerosol load by using the AVHRR TIR signals. The method is similar to the retrieval of cirrus using the brightness temperature difference (Wu, 1987; Giraud et al., 1997). Ackerman (1997) investigated in theory the possibility of detecting aerosols using the 8.5, 11 and 12 μm signals.

Zhang et al. (2006) pointed out that the signals of these three TIR channels can be simulated with a forward radiative transfer model if adequate aerosol physical parameters (complex refraction index, particle size distribution and particle shape) are chosen. Calculations show that T_{11} has a quasi-linear relationship with dust optical thickness, and ΔT a quasi-linear relationship with particle size. Based on this understanding, Zhang et al. developed an algorithm for the retrieval of dust optical thickness and particle effective radius of dust storm. Dust load is then calculated from dust optical thickness. Zhang

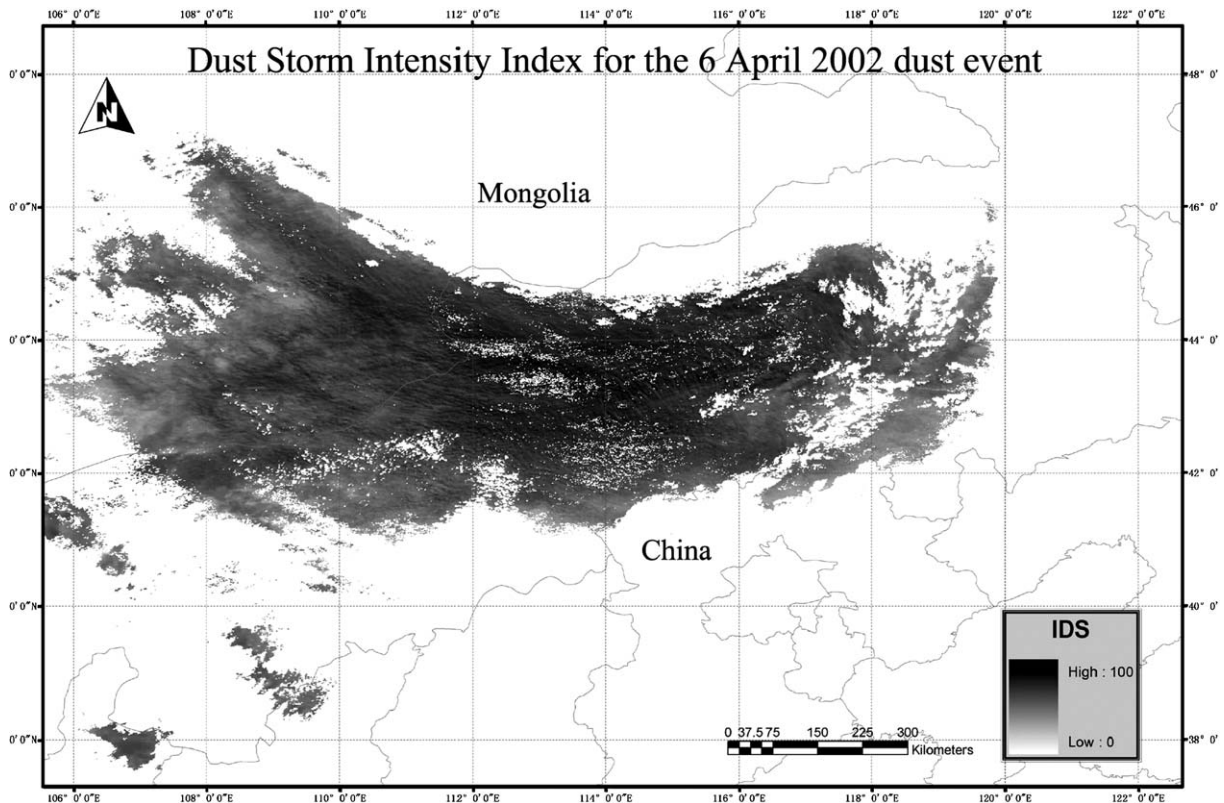


Fig. 11. An example of dust storm intensity index I_{ds} using the FY-1D polar orbiting satellite data for the 6 April 2002 dust event.

et al. made the following assumptions: (1) complex refractive index (an index describing the interaction of radiation and matter, its real part describes the scattering properties and the imaginary part the absorption properties of matter) is as given by Koepke et al. (1997) and Gu et al. (2003); (2) dust particle size distribution is lognormal and (3) dust particles are spherical. Under these assumptions, the single scattering albedo, asymmetry factor, and extinction coefficient ratio of the dust layer can be calculated from the Mie model. Further, for given dust optical thickness, the satellite observation can be simulated for arbitrary wavelengths using the DISORT model (Stamnes et al., 1988).

Several other assumptions are made to simplify the calculation. These are (1) the underlying surface is homogeneous; (2) the dust cloud is a single layer parallel to the surface; (3) the atmospheric layers above and below the dust layer are clear windows and (4) the dust layer fully fills the observation field. Then, the observed radiance in a given channel I_i can be expressed as

$$I_i = \varepsilon_i B_\lambda(T_c) + t_i B_\lambda(T_s) \quad (18)$$

where ε_i and t_i are emissivity and transmissivity of the dust layer at the channel wavelength, T_s and T_c are the

underlying surface temperature and dust-cloud-top equivalent temperature, respectively.

Under the assumptions, the calculations show that T_{11} and ΔT are determined by T_s , T_c and optical thickness (representing dust load). If T_s and T_c are fixed then T_{11} has a linear relationship with dust optical thickness and ΔT a linear relationship with dust particle size. Thus, the optical thickness and particle effective radius can be retrieved from satellite signal simultaneously.

Fig. 12 shows the retrieval results for dust optical thickness at 0.55 μm (Fig. 12a), particles effective radius in μm (Fig. 12b) and dust load in $10^6 \mu\text{g m}^{-2}$ (Fig. 12c). However, the retrieval results require more validations with measurements.

5. Concluding remarks

We have attempted to summarise some of the achievements in studies on Asian dust climatology, dust storm modeling and dust storm monitoring.

Asian dust climatology is well documented in terms of dust storm frequency, distribution and seasonal variations. The synoptic systems for the generation of severe dust storms are well known. This

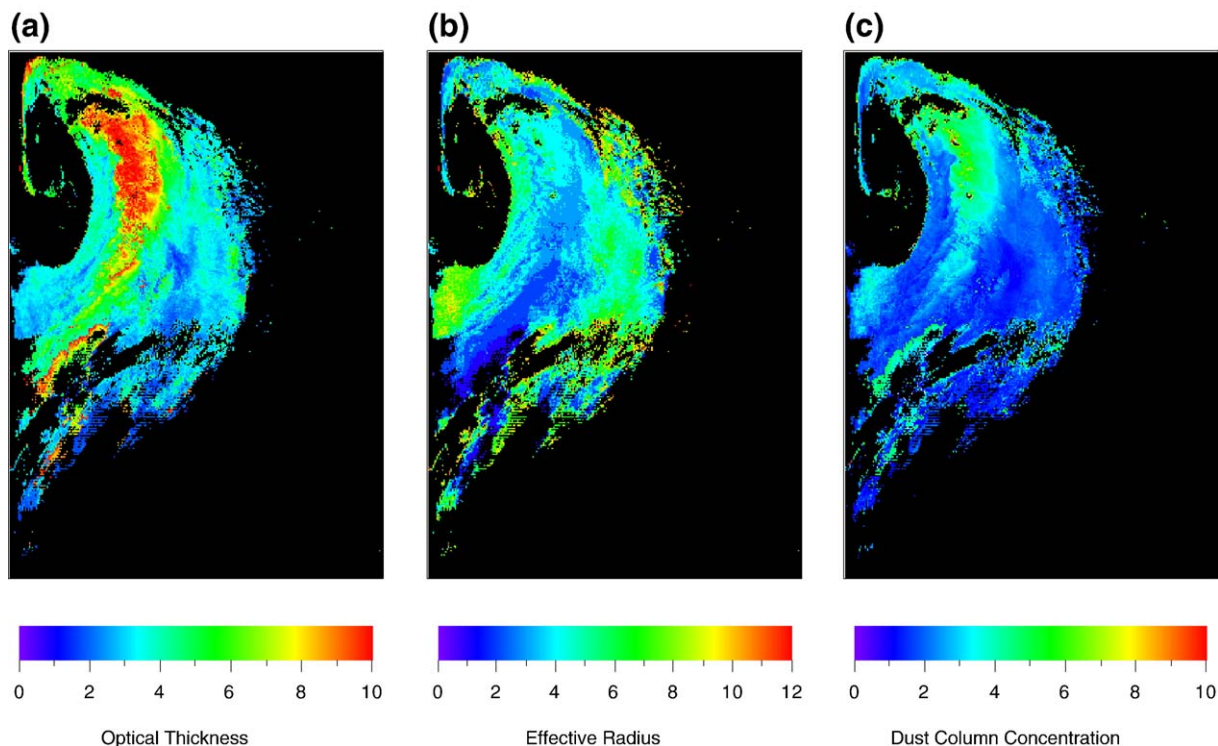


Fig. 12. An example of estimated dust optical thickness, effective dust particle radius and dust load for the 7 April 2001 dust storm, retrieved from MODIS data.

knowledge is important for operational dust forecast and provides the necessary background for dust modeling. Historical observations and recent experience show that the annual variability of Asian dust is substantial. This is so far poorly understood. The long-term variability of Asian dust is closely related to that of global circulation, and at the same time, an indicator of climate change. Therefore, in depth investigation on the long-term dust storm variability is helpful to better understanding climate change. Zhang et al. (2006) presented an analysis on how Asian dust-storm frequency is related to Arctic ice cover, but much more research is desirable.

The achievements in dust modeling are significant, but many problems remain. The main ones are as follows:

- (1) The existing dust models have skill in predicting the outbreak and evolution of Asian dust storms. Progress has been made in quantitative computation of dust concentration, emission and deposition etc. probably with the right order of magnitude. However, the uncertainties of the model predictions are large. We have almost no direct measurements of dust fluxes and it is difficult to assess the uncertainties of the dust emission schemes.
- (2) Improvements to dust-model components are necessary, such as dust-emission, dust-deposition and convective transport schemes. Jung et al. (2005) showed that wet deposition and convective transport are important to Asian dust modeling. Again, there is a critical lack of direct dry- and wet-deposition measurements for model validation and we know little about in-cloud wet removal.
- (3) Dust emission varies greatly in space and time, depending on both atmospheric and land-surface conditions. From satellite imagery, one often sees “point source” plumes which result in wide spread dust weather. Thus only a small area of the surface may be eroding even under conditions when the surface is relatively uniform. Small differences in conditions can result in huge differences in emission. The resolutions of atmospheric models are typically 10 to 100 km, too coarse to represent the spatial variations of dust emission (Liu and Westphal, 2001). To overcome this problem, subgrid closure schemes accounting for the spatial variability in land-surface and atmospheric conditions are required. The mosaic approach of representing land-surface heterogeneity is useful to dust modeling. We are not aware of any good method for describing the subgrid variation of friction velocity.
- (4) Land-surface parameters are required for dust modeling. In dust-emission and deposition schemes, friction velocity u_* is a key quantity. The calculations of u_* and u_{*t} depend on aerodynamic roughness length z_0 (Marticorina and Bergametti, 1995). Laurent et al. (2005) presented an interesting method of deriving z_0 from the POLDER/ADEOS-1 surface products. Further test of the method is nevertheless required.
- (5) Another quantity of critical importance to dust modeling is parent soil particle-size data (Shao, 2001, 2004), but a database of parent soil particle-size distribution is yet to be established.
- (6) Only limited dust-concentration data are available for model validation. Dust concentration can be converted from visibility using empirical relationships, but the quality of the data is low because visibility depends not only on dust concentration, but also on particle size and atmospheric qualities such as air humidity and because visibility is a subjective measure. The advantage of the data is the broad spatial coverage and regular temporal coverage. Dust concentration measurements are also available from high- and low-volume samplers. These measurements are probably the most accurate, but are poor in spatial and temporal resolution, because there are very few samplers and a measurement takes days even weeks. In the dust-affected areas of Asia, a network of lidar is now functioning which produces aerosol profile observations (Sugimoto et al., 2003; Shimizu et al., 2004). Lidar data are nevertheless indirect and are limited to some locations. During dust events, lidar only provides information for the lower part of the atmosphere, as lidar signals often cannot penetrate the dense dust layer. Satellite remote sensing offers an important source of data. However, technical difficulties in converting satellite signals to practically useful physical quantities, such as dust load are not yet solved.
- (7) Data assimilation is a technique successfully implemented in atmospheric and oceanic modeling. Progress in remote sensing technology and inverse data analysis techniques may enable the assimilation of dust measurements into dust modeling in the near future. Preliminary work has been done by Nickovic et al. (2003) using lidar measurements. However, the amount of

data they used is very limited. In 2002, CMA established a dust monitoring network in China. At the network stations, radiation and dust measurements are made. It is hopeful that assimilation of dust measurements into dust modeling will become possible with the increased amount of dust observations of various sources.

It is reasonable to conclude that recent progress in satellite remote sensing technology and data analysis have enabled the successful identification of dust storms from satellite imagery. There are however obvious difficulties in detecting dust storms under cloud cover. It is necessary to combine conventional observation with satellite data to provide an adequate dust monitoring system.

Estimates of dust-related physical quantities are more difficult, because the signals detected by satellites are mixture of radiation signals from the land surface, clouds, dust and other aerosol. As discussed in Section 4, however, under assumptions, it is possible to derive useful information from satellite data, such as dust load and effective particle size. Much more in depth research is nevertheless needed.

It is not too hopeful to determine dust-related quantities accurately from satellite data alone. To explore the possibilities how satellite data can be used in combination with other radiation measurements is promising. For example, Gai et al. (2006) used sun photometers to estimate dust optical thickness in the Tarim Basin. In 2002, CMA established a ground based dust-storm monitoring network. Ground-based radiation measurements can be used to determine dust optical thickness which is directly comparable with that derived from satellite data. Further, integrated dust-storm prediction models are providing useful estimates of dust distribution, dust particle size, surface radiative temperature, soil moisture etc. To our knowledge, such data are not yet effectively used in satellite remote sensing studies. We should explore how numerical models can provide input data for the inverse calculation using satellite data.

Acknowledgments

This study is supported by the Ministry of Finance of China Project Y0101 “Monitoring and prediction of soil moisture and dust storms in Northwest China” and by a grant from the Research Grants Council of the Hong

Kong Special Administrative Region China [Project No. City U 101903]. We are grateful to Prof. R. Arimoto and Prof. J. Prospero for their comments on a draft of this paper.

References

- Ackerman, S., 1989. Using the radiative temperature difference at 3.7 and 11 μm to track dust outbreaks. *Remote Sens. Environ.* 27, 129–133.
- Ackerman, S., 1997. Remote sensing aerosols using satellite infrared observations. *J. Geophys. Res.* 102, 17069–17079.
- Alfaro, S.C., Gomes, L., 2001. Modelling mineral aerosol production by wind erosion: emission intensities and aerosol size distributions in source areas. *J. Geophys. Res.* 106, 18075–18084.
- Arimoto, R., Kim, Y.J., Kim, Y.P., Quinn, P.K., Bates, T.S., Anderson, T.L., Gong, S., Uno, I., Chin, M., Huebert, B.J., Clarke, A.D., Shinozuka, Y., Weber, R.J., Anderson, S.J.R., Guazzotti, A., Sullivan, R.C., Sodeman, D.A., Prather, K.A., Sokolik, I., 2006. Characterization of Asian dust during ACE-Asia. *Glob. Planet. Change* 52, 23–56.
- Carlson, T.N., 1979. Atmospheric turbidities in Saharan dust outbreaks as determined by analysis of satellite brightness data. *Mon. Weather Rev.* 107, 322–335.
- Chatenet, B., Marticorena, B., Gomes, L., Bergametti, G., 1996. Assessing the microped size distributions of desert soils erodible by wind. *Sedimentology* 43, 901–911.
- Chun, Y.S., Boo, K.O., Kim, J., Park, S., Lee, M., 2001. Synopsis, transport and physical characteristics of Asian dust in Korea. *J. Geophys. Res.* 106, 18461–18469.
- Christensen, J.H., 1997. The Danish Eulerian hemispheric model — a three-dimensional air pollution model used for the arctic. *Atmos. Environ.* 31, 4169–4191.
- DeFries, R.S., Townshend, J.R.G., 1994. NDVI-derived land cover classification at a global scale. *Int. J. Remote Sens.* 15, 3567–3586.
- Gai, C.S., Li, X.Q., Zhao, F.S., 2006. Mineral aerosol properties observed in the northwest region of China. *Glob. Planet. Changes* 52, 173–181.
- Gao, Y., Arimoto, R., Duce, R.A., Zhang, X.Y., Zhang, G.Y., An, Z.S., Chen, L.Q., Zhou, M.Y., Gu, D.Y., 1997. Temporal and spatial distributions of dust and its deposition to the China Sea. *Tellus* 49B, 172–189.
- Gillette, D.A., Hanson, K.J., 1989. Spatial and temporal variability of dust production caused by wind erosion in the United States. *J. Geophys. Res.* 94D, 2197–2206.
- Gillette, D.A., Passi, R., 1988. Modeling dust emission caused by wind erosion. *J. Geophys. Res.* 93, 14233–14242.
- Giraud, V., Buriez, J.C., Fouquart, Y., Parol, F., 1997. Large-scale analysis of cirrus clouds from AVHRR data: assessment of both a microphysical index and the cloud-top temperature. ??
- Ginoux, P., Chin, M., Tegen, I., Prospero, J., Holben, B., Dubovik, O., Lin, S.J., 2001. Sources and distribution of dust aerosols simulated with the GOCART model. *J. Geophys. Res.* 106, 20255–20273.
- Ginoux, P., Prospero, J., Torres, O., Chin, M., 2004. Long-term simulation of global dust distribution with the GOCART model: correlation with North Atlantic Oscillation. *Environ. Model. Softw.* 19, 113–128.
- Giorgi, F.A., 1986. Particle dry-deposition parameterization scheme for use in tracer transport models. *J. Geophys. Res.* 91, 9794–9806.

- Giorgi, F., Chameides, W.L., 1986. Rainout lifetimes of highly soluble aerosols and gases as inferred from simulations with a general circulation model. *J. Geophys. Res.* 91, 14367–14376.
- Gomes, L., Bergametti, G., Dulac, F., Ezat, U., 1990. Assessing the actual size distribution of atmospheric aerosols collected with a cascade impactor. *J. Aerosol Soc.* 21, 47–59.
- Gong, S.L., Zhang, X.Y., Zhao, T.L., McKendry, I.G., Jaffe, D.A., Lu, N.M., 2003. Characterization of soil dust aerosol in China and its transport and distribution during 2001 ACE-Asia. 2. Model simulation and validation. *J. Geophys. Res.* 108, 4262, doi:10.1029/2002JD002633.
- Griggs, M., 1975. Measurements of atmospheric aerosol optical thickness over water using ERTS-1 data. *J. Air Pollut. Control Assoc.* 25, 622–626.
- Gu, Y., Rose, W.I., Bluth, G.J.S., 2003. Retrieval of mass sizes of particles in sandstorms using two MODIS IR bands: A case study of April 7, 2001 sandstorm in China. *Geophys. Res. Lett.* 30 (15), 1805–1808.
- Han, Z., Ueda, H., Matsuda, K., Zhang, R., Arao, K., Kanai, Y., Hasome, H., 2004. Model study on particle size segregation and deposition during Asian dust events in March 2002. *J. Geophys. Res.* 109, D19205, doi:10.1029/2004JD004920.
- Husar, R.B., et al., 2001. Asian dust events of April 1998. *J. Geophys. Res.* 106, 18317–18330.
- In, H.J., Park, S.U., 2003. The soil particle size dependent emission parameterization for an Asian dust observed in Korea in April 2002. *Atmos. Environ.* 37, 4625–4636.
- Joussaume, S., 1990. Three-dimensional simulation of the atmospheric cycle of desert dust particles using a general circulation model. *J. Geophys. Res.* 95, 1909–1941.
- Jung, E.J., Shao, Y., Sakai, T., 2005. A study on the effects of convective transport on regional-scale Asian dust storms in 2002. *J. Geophys. Res.* 110 (D20), D20201, doi:10.1029/2005JD005808.
- Koepke, P., Hess, M., Schult, I., Shettle, E.P., 1997. Global Aerosol Data Set. Report No. 243, Max-Planck-Institut für Meteorologie, Hamburg, ISSN 0937-1060.
- Kurosaki, Y., Mikami, M., 2003. Recent frequent dust events and their relation to surface wind in East Asia. *Geophys. Res. Lett.* 30 (14), 1736, doi:10.1029/2003GL017261.
- Kurosaki, Y., Mikami, M., 2005. Regional difference in the characteristics of dust event in East Asia: relationship among dust outbreak, surface wind, and land surface condition. *J. Meteorol. Soc. Jpn.* 83A, 1–8.
- Laurent, B., Marticorena, B., Bergametti, G., Chazette, P., Maignan, F., Schmechtig, C., 2005. Simulation of the mineral dust emission frequencies from desert areas of China and Mongolia using an aerodynamic roughness length map derived from the POLDER/ADEOS-1 surface products. *J. Geophys. Res.* 110, D18504, doi:10.1029/2004JD005013.
- Littmann, T., 1991. Dust storm frequency in Asia: climatic control and variability. *Int. J. Climatol.* 11, 393–412.
- Liu, M., Westphal, D.L., 2001. A study of the sensitivity of simulated mineral dust production to model resolution. *J. Geophys. Res.* 106, 18099–18112.
- Liu, M., Westphal, D.L., Wang, S., Shimizu, A., Sugimoto, N., Zhou, J., Chen, Y., 2003. A high-resolution numerical study of the Asian dust storms on April 2001. *J. Geophys. Res.* 108, 8653, doi:10.1029/2002JD003178.
- Mahowald, N., Kohfeld, K., Hansson, M., Balkanski, Y., Harrison, S.P., Printice, I.C., Schulz, M., Rodhe, H., 1999. Dust sources and deposition during the last glacial maximum and current climate: a comparison of model results with paleodata from ice cores and marine sediments. *J. Geophys. Res.* 104, 15895–15916.
- Mahowald, N.M., Luo, C., del Corral, J., Zender, C.S., 2003. Interannual variability in atmospheric mineral aerosols from a 22-year model simulation and observational data. *J. Geophys. Res.* 108, doi:10.1029/2002JD002821.
- Marticorena, B., Bergametti, G., 1995. Modeling the atmospheric dust cycle. 1. Design of a soil-derived dust emission scheme. *J. Geophys. Res.* 100, 16,415–16,430.
- Mikami, M., Shi, G.Y., Yabuki, S., Aoki, T., Iwasaka, Y., Uchiyama, A., Yasui, M., Uno, I., Tanaka, T.Y., Kurosaki, Y., Sakai, T., Seino, N., Takemi, T., Nakawo, M., Kanayama, S., Fujita, K., Hayashi, M., Masuda, K., Matsuki, A., Abe, O., Du, M., Tsutsumi, Y., Yamada, Y., Chiba, M., Zhang, R.J., Zhang, X.Y., Shen, Z., Wei, W., 2006. Aeolian dust experiment on climate impact: An overview of Japan-China joint project ADEC. *Glob. Planet. Change* 52, 142–172.
- Mikami, M., Osamu, A., Du, M.Y., Chiba, O., Fujita, K., Hayashi, M., Iwasaka, Y., Kai, K., Masuda, K., Nagai, T., Ootomo, T., Suzuki, J., Uchiyama, A., Yabuki, S., Yamada, Y., Yasui, M., Shi, G.Y., Zhang, X.Y., Shen, Z.B., Wei, W.S., Zhou, J., 2002. The impact of aeolian dust on climate: Sino-Japanese Cooperative Project ADEC. *J. Arid Land Studies* 11, 211–222.
- Natsagdorj, L., Jugder, D., Chung, Y.S., 2003. Analysis of dust storms observed in Mongolia during 1937–1999. *Atmos. Environ.* 37, 1401–1411.
- Nickling, W.G., McTainsh, G.H., Leys, J.F., 1999. Dust emissions from the Channel Country of western Queensland, Australia. *Z. Geomorphol. N. F.* 116, 1–17.
- Nickovic, S., Wilson, W.E., Sassen, K., Sugimoto, N., Malm, W.C., 2001. Asian dust events of April 1998. *J. Geophys. Res.* 106, 18317–18330.
- Nickovic, S., Music, S., Ansmann, A., 2003. DREAM dust model: ongoing and future developments. 2nd Workshop on Mineral Dust, Paris, 10–12 September 2003.
- Norton, C., Mosher, F.R., Hinton, B., Martin, D.W., Santok, D., Kuhlow, W., 1980. A model for calculating desert aerosol turbidity over the oceans from geostationary satellite data. *J. Appl. Meteorol.* 19, 633–644.
- Park, S.U., In, H.J., 2003. Parameterization of dust emission for the simulation of the Yellow Sand (Asian dust) event observed in March 2002 in Korea. *J. Geophys. Res.* 108, 4618, doi:10.1029/2003JD003484.
- Parungo, F., Li, Z., Li, X., Yang, D., Harris, J., 1994. Gobi dust storms and the great green wall. *Geophys. Res. Lett.* 21, 999–1002.
- Perlwitz, J., Tegen, I., Miller, R.L., 2001. Interactive soil dust aerosol model in the GISS GCM: 1. Sensitivity of the soil dust cycle to radiative properties of soil dust aerosols. *J. Geophys. Res.* 106, 18,167–18,192.
- Prospero, J.M., Ginoux, P., Torres, O., Nicholson, S.E., Gill, T.E., 2002. Environmental characterization of global sources of atmospheric soil dust identified with the NIMBUS 7 Total Ozone Mapping Spectrometer (TOMS) absorbing aerosol product. *Rev. Geophys.* 40, 2–31.
- Qian, W., Quan, L., Shi, S., 2002. Variations of the dust storm in China and its climatic control. *J. Climatol.* 15, 1,216–1,229.
- Raupach, M.R., 1992. Drag and drag partition on rough surfaces. *Boundary-Layer Meteorol.* 60, 375–395.
- Seinfeld, J.H., Pandis, S.N., 1998. *Atmospheric Chemistry and Physics. From Air Pollution to Climate Change.* John Wiley and Sons, New York.

- Seino, N., Sasaki, H., Yamamoto, A., Mikami, M., Zhou, H., Zeng, F., 2005. Numerical simulation of meso-scale circulation in the Tarim Basin associated with dust events. *J. Meteorol. Soc. Jpn.* 83A, 205–218.
- Shao, Y., 2000. *Physics and Modelling of Wind Erosion*. Kluwer Academic Publishers, 393pp.
- Shao, Y., 2001. A model for mineral dust emission. *J. Geophys. Res.* 106, 20,239–20,254.
- Shao, Y., 2004. Simplification of a dust emission scheme and comparison with data. *J. Geophys. Res.* 109, D10202, doi:10.1029/2003JD004372.
- Shao, Y., Leslie, L.M., 1997. Wind erosion prediction over the Australian continent. *J. Geophys. Res.* 102, 30,091–30,105.
- Shao, Y., Wang, J.J., 2003. A climatology of northeast Asian dust events. *Meteorol. Z.* 12, 175–183.
- Shao, Y., Raupach, M.R., Findlater, P.A., 1993. The effect of saltation bombardment on the entrainment of dust by wind. *J. Geophys. Res.* 98, 12,719–12,726.
- Shao, Y., et al., 2003. Real-time numerical prediction of northeast Asian dust storms using an integrated modeling system. *J. Geophys. Res.* 108, 4691, doi:10.1029/2003JD003667.
- Shenk, W.E., Curran, R.J., 1974. The detection of dust storms over land and water with satellite visible and infrared measurements. *Mon. Weather Rev.* 102, 830–837.
- Shimizu, A., Sugimoto, N., Matsui, I., Arao, K., Uno, I., Murayama, T., Kagawa, N., Aoki, K., Uchiyama, A., Yamazaki, A., 2004. Continuous observations of Asian dust and other aerosols by polarization lidars in China and Japan during ACE-Asia. *J. Geophys. Res.* 109, doi:10.1029/2002JD003253.
- Stamnes, K., Tsay, S.C., Wiscombe, W., Jayaweera, K., 1988. Numerically stable algorithm for discrete-ordinate-method radiative transfer in multiple scattering and emitting layered media. *Appl. Opt.* 27 (12), 2502–2509.
- Sugimoto, N., Uno, I., Nishikawa, M., Shimizu, A., Matsui, I., Dong, X., Chen, Y., Quan, H., 2003. Record heavy Asian dust in Beijing in 2002: observations and model analysis of recent events. *Geophys. Res. Lett.* 30, 1640, doi:10.1029/2002GL016349.
- Sun, J., Zhang, M., Liu, T., 2001. Spatial and temporal characteristics of dust storms in China and its surrounding regions, 1901–1999: relations to source area and climate. *J. Geophys. Res.* 106, 10,325–10,333.
- Tanaka, T.Y., Chiba, M., 2006. A numerical study of the contributions of dust source regions to the global dust budgets. *Glob. Planet. Change* 52, 88–104.
- Tanaka, T.Y., Orito, K., Sekiyama, T.T., Shibata, K., Chiba, M., Tanaka, H., 2003. MASINGAR, a global tropospheric aerosol chemical transport model coupled with MRI/JMA98 GCM: model description. *Pap. Meteor. Geophys.* 53, 119–138.
- Tanré, D., et al., 1997. Remote sensing of aerosol over oceans from EOS-MODIS. *J. Geophys. Res.* 102, 16971–16988.
- Tegen, I., Fung, I., 1994. Modeling of mineral dust in the atmosphere: sources, transport, and optical thickness. *J. Geophys. Res.* 99, 22,897–22,914.
- Tegen, I., Harrison, S.P., Kohfeld, K., Prentice, I.C., Coe, M., Heimann, M., 2002. Impact of vegetation and preferential source areas on global dust aerosol: results from a model study. *J. Geophys. Res.* 107, 4576, doi:10.1029/2001JD000963.
- Tegen, I., Werner, M., Harrison, S.P., Kohfeld, K.E., 2004. Relative importance of climate and land use in determining present and future global soil dust emission. *Geophys. Res. Lett.* 31, L05105, doi:10.1029/2003GL019216.
- Uno, I., Amano, H., Emori, S., Kinoshita, K., Matsui, I., Sugimoto, N., 2001. Trans-Pacific yellow sand transport observed in April 1998: a numerical simulation. *J. Geophys. Res.* 106, 18331–18344.
- Uno, I., et al., 2003. Regional chemical weather forecasting system CFORS: model descriptions and analysis of surface observations at Japanese island stations during the ACE-Asia experiment. *J. Geophys. Res.* 108, 8668, doi:10.1029/2002JD002845.
- Uno, I., Harada, K., Satake, S., Hara, Y., Wang, Z., 2005. Meteorological characteristics and dust distribution of the Tarim Basin simulated by the nesting RAMS/CFORS dust model. *J. Meteorol. Soc. Jpn.* 83A, 219–239.
- Wang, S.G., Yang, D.B., Jing, J., Xu, Q.Y., Yang, Y.F., 1995. Study on the formative causes and countermeasures of the catastrophic sandstorm occurred in northwest China. *J. Desert Res.* 15, 19–30.
- Wang, Z., Ueda, H., Huang, M., 2000. A deflation module for use in modeling long-range transport of yellow sand over east Asia. *J. Geophys. Res.* 105, 26947–26957.
- Wen, S., Rose, W.I., 1994. Retrieval of sizes and total masses of particles in volcanic clouds using AVHRR bands 4 and 5. *J. Geophys. Res.* 99, 5421–5431.
- Wesely, M.L., 1989. Parameterization of surface resistances to gaseous dry deposition in regional-scale numerical models. *Atmos. Environ.* 23, 1,293–1,304.
- Wesely, M.L., Cook, D.R., Hart, R.L., Speer, R.E., 1985. Measurements and parameterization of particulate sulfur dry deposition over grass. *J. Geophys. Res.* 90, 2,131–3,143.
- Westphal, D.L., Toon, O.B., Carson, T.N., 1988. A case study of mobilisation and transport of Saharan dust. *J. Atmos. Sci.* 45, 2,145–2,175.
- White, B., 1979. Soil transport by winds on Mars. *J. Geophys. Res.* 84, 4643–4651.
- Woodward, S., 2001. Modeling the atmospheric lifecycle and radiative impact of mineral dust in the Hadley Centre climate model. *J. Geophys. Res.* 106, 18,155–18,166.
- Wu, M.L., 1987. A method for remote sensing the emissivity, fractional cloud cover and cloud top temperature of high-level, thin clouds. *J. Clim. Appl. Meteorol.* 26, 225–233.
- Zender, C.S., Bian, H., Newman, D., 2003. Mineral Dust Entrainment and Deposition (DEAD) model: description and 1990s dust climatology. *J. Geophys. Res.* 108, 4416, doi:10.1029/2002JD002775.
- Zhang, L., Gong, S.L., Padro, J., Barrie, L., 2001. A size-segregated particle dry deposition scheme for an atmospheric aerosol module. *Atmos. Environ.* 35, 549–560.
- Zhang, P., Lu, N.M., Hu, X.Q., Dong, C.H., 2006. Identification and physical retrieval of dust storm using three MODIS thermal IR channels. *Glob. Planet. Change* 52, 197–206.
- Zhao, Y.L., Gong, S.L., Zhang, X.Y., McKendry, I.G., 2003. Modeled size-segregated wet and dry deposition budgets of soil dust aerosol during ACE-ASIA 2001: implications for trans-Pacific transport. *J. Geophys. Res.* 108, 8665, doi:10.1029/2002JD003363.
- Zheng, X.J., Lu, W.J., Luo, J.N., 2001. Research on duststorm monitoring using multi-channel meteorological satellite data. *J. Remote Sens.* 5, 300–305.
- Zhou, Z.J., 2001. Blowing sand and sand storm in China in recent 45 years. *Quat. Sci.* 21, 9–17.